Design and fabrication of a cryogenic magnetocaloric composite by spark plasma sintering based on the RAl_2 Laves phases (R= Ho, Er)

J.L. Sánchez Llamazares,[a,*] J. Zamora,[a] C.F. Sánchez-Valdés,[b,**] P. Álvarez-Alonso[c]

[a]*Instituto Potosino de Investigación Científica y Tecnológica A.C., Camino a la Presa San José 2055, Col. Lomas 4ª, San Luis Potosí, S.L.P. 78216, México.*
[b]*División Multidisciplinaria, Ciudad Universitaria, Universidad Autónoma de Ciudad Juárez (UACJ), calle José de Jesús Macías Delgado # 18100, Ciudad Juárez, Chihuahua, México.*
[c]*Departamento de Física, Universidad de Oviedo, Calvo Sotelo s/n, 33007 Oviedo, Spain.*

Abstract. We report the design and fabrication of a highly dense (>97 %) two-phase magnetocaloric composite operating in the cryogenic temperature range based on the binary Laves phases $HoAl_2$ and $ErAl_2$ with a nearly table-like magnetic entropy change curve $\Delta S_M(T)$ at 2 T. Such particular $\Delta S_M(T)$ dependence was obtained, from the individual $\Delta S_M(T)$ curves of the precursors, for the composition 28 wt.% ($ErAl_2$) + 72 wt.% ($HoAl_2$). This composition was selected to make a composite by spark plasma sintering from homogeneously mixed melt-spun ribbons of both intermetallic compounds. The calculated and experimental $\Delta S_M(T)$ curves obtained for the as-sintered composite were found to be similar. Our results highlight the potential of this processing metallurgical technique for producing two-phase active magnetic regenerators with a designed entropy change curve for specific magnetic refrigeration applications.

Keywords: magnetocaloric effect; two-phase magnetocaloric composite; RAl_2 Laves phases; spark plasma sintering.

[*]Corresponding author. Email address: jose.sanchez@ipicyt.edu.mx (J.L. Sánchez Llamazares).
[**] Corresponding author. Email address: cesar.sanchez@uacj.mx (C.F. Sánchez Valdés).

1. Introduction

The Ericsson-type magnetic refrigeration cycle, that consists of two isothermal and two isomagnetic field processes, shows its optimal energy efficiency for table-like shaped magnetic entropy $\Delta S_M(T)$ [1]. Hence, the development of materials exhibiting such peculiar feature is an important technological issue linked to magnetic refrigeration applications. However, the general shape of the $\Delta S_M(T)$ curve for a single magnetocaloric (MC) material through its second- or first-order transition is usually referred as either caret- or sharp asymmetrical "half-dome" or skyscraper-like shaped, respectively [1-2]. Therefore, the design of a composite material based on two or more magnetocaloric phases is the most practical way to fulfill the above-mentioned requirement for which the spanning of the temperature interval for the magnetocaloric effect curves also leads to other desirable features such as the widening of the working temperature range, usually given by the temperature interval delimited by the full-width at half-maximum δT_{FWHM} of $\Delta S_M(T)$, and the increase of the refrigerant capacity *RC*. Considering that the maximum entropy change $|\Delta S_M|^{max}$ decreases with the increase of the number of components, most of the magnetocaloric composites reported are limited to two phases. In addition, we shall focus on biphasic composites based on two ferromagnetic materials.

In practice, there are two kinds of MC composites; in some systems, the synthesis process and the chosen composition lead to the coexistence of two or more magnetic phases in the same material with different transition temperatures, which lead to the widening of the $\Delta S_M(T)^{comp}$; in some cases, a rough nearly constant magnetic entropy change curve is found [3-8]. But the most important MC composites are those that are intentionally formed by two or more different independent phases appropriately chosen to obtain a desired constant $\Delta S_M(T)^{comp}$ curve in a predetermined temperature range as reported by some groups [9-14]. Some of these materials are not intrinsically integrated, they simply result from putting the independent parts together [11-14].

If the task is the attainment of a biphasic MC composite based on two ferromagnetic materials, such as A and B, with a designed table-like or flattened $\Delta S_M(T)^{comp}$ curve for a required temperature interval and magnetic field change $\mu_o\Delta H$, one must consider their weight fraction *x*, since $\Delta S_M(T, \mu_o\Delta H, x)^{comp} = x\,\Delta S_M^A(T, \mu_o\Delta H) + (1-x)\,\Delta S_M^B(T, \mu_o\Delta H)$ where $0 \le x \le 1$, and the particular characteristics of their $\Delta S_M(T)$ curves [15]: the temperature at which the maximum of the $\Delta S_M(T)$ curve appears (located nearby the Curie temperature T_C), the difference $\Delta T_C = |T_C^A - T_C^B|$ between both phases (because the flattening will appear between the respective T_C), the

height of the curve (given by $|\Delta S_M|^{max}$), and its asymmetric shape below and above T_C. Several authors have discussed the influence of these factors in the resulting $\Delta S_M(T)^{comp}$, providing general guidelines to optimize the magnetic entropy change [12, 14, 16]. But in reality, the most realistic way to design a composite with the desired $\Delta S_M(T)^{comp}$ is to obtain experimentally $\Delta S_M^A(T)$ and $\Delta S_M^B(T)$ for the $\mu_o \Delta H$ value of interest to numerically compute the resulting $\Delta S_M(T)^{comp}$ by the simple summation varying x in the whole range to find the weight fraction x that provides a flattened $\Delta S_M(T)^{comp}$ (see, for instance, Refs. 12, 13 and 16).

In this work, we focused on the design and fabrication by spark plasma sintering (SPS) of a two-phase MC composite with a table-like entropy change curve in the cryogenic temperature range based on the binary intermetallic Laves phases $HoAl_2$ and $ErAl_2$. It is well known that some rare-earth-based intermetallic compounds that favorably combine a high saturation magnetization with a moderate specific heat show the best properties as magnetic refrigerants in the cryogenic temperature range [1-2, 17-21]. Among them, the binary Laves phases RM_2 with R= Tb, Dy, Ho and Er, and M= Al or Ni, show a large MC effect [22]; moreover, they are very stable and easy to produce compounds. We have chosen $HoAl_2$ and $ErAl_2$ to develop this work. They are collinear ferromagnets that crystallize into the cubic $MgCu_2$-type crystal structure of the Laves phases (C15, space group *Fd m*) [23-25]. For $HoAl_2$, values of Curie temperature of 27 K [26] and 31.5 K [27] have been reported, and for $ErAl_2$ T_C= 13 K [28-29]. Both compounds have showed a large MC effect [22, 27, 30-32].

The use of conventional sintering for shaping and consolidating multiphase MC composites was first proposed by *Hashimoto et al*. [9-10], who fabricated a tri-layered structure by sintering based on RAl_2 phases with R= Dy, Ho, and Er. However, it is difficult to fabricate a two-phase material for Ericsson cycle-based applications by conventional sintering since, as a rule, long-term high sintering temperatures are needed to reach a highly dense sintered material and the diffusion will promote a strong solid-state reaction between the mixed phases that forms additional phases with the consequent change of the initial phase constitution. In this sense, SPS leads to the consolidation of the parent specimens in a much shorter time and therefore is a considerably advantageous alternative to form bi- or mult-iphasic composites. In this process, small sample pieces, inside a graphite die, are under the simultaneous application of uniaxial pressure and heating by a pulsed high-intensity electrical current, giving rise to a highly-dense solid piece with a pre-established shape obtained in a relatively shorter time and lower temperatures in comparison with conventional sintering [33-34].

SPS has been used to consolidate several MC materials such as La(Fe,Si)$_{13}$-type [35-38], hexagonal Fe_2P-type compounds [39-42] and MnFeSi [43]. However, spark plasma sintering has been scarcely used as a processing route to fabricate magnetocaloric composites with the exception of the work carried out by *Yue et al*. [44], who used it to join two large cuboid samples of Gd and $Gd_5Si_2Ge_2$ to produce a layered structure of $Gd_x(Gd_5Si_2Ge_2)_{1-x}$ with x = 0.3, 0.5, and 0.7.

In this work, we show the potential of this technique to consolidate MC composites with the desired $\Delta S_M(T)^{comp}$ dependence previously computed from the entropy change curves of the precursors. However, instead of using powders, we have chosen melt-spun ribbon flakes that were homogeneously mixed before sintering. Hence, the formation of a solid solution of both materials will be limited to a thin layer boundary whose volume can be negligible with respect to the total volume of the two components.

2. Experimental procedure

Ingots of the intermetallic compounds $HoAl_2$ and $ErAl_2$ were obtained by arc-melting of elemental constituents in a titanium-gettered inert Ar atmosphere. As raw materials, high purity elements were used: Al (99.999 %; Alfa Aesar), and Ho and Er (99.9 %; Sigma Aldrich). Samples were remelted several times to ensure a good starting chemical homogeneity. From the master ingots, pieces of melt-spun ribbons were obtained by rapid solidification in an Ar atmosphere at a linear speed of the copper wheel of 20 m/s (for both alloys); initially the ribbons had the following typical dimensions: 1.1-1.3 mm width and 7-14 mm length. For this process, an Edmund Bühler model SC melt spinner system was used. The spark plasma sintering process is described in the section 3.2.

X-ray diffraction (XRD) analyses were performed in a high-resolution Rigaku Smartlab diffractometer with Cu-$K_{\alpha1}$ radiation ($\lambda_{\alpha1}$ = 1.5405 Å). XRD patterns were collected at room temperature on samples finely powdered with an agate mortar. Structural analysis was performed using the FullProf suite [45]. Microstructure and elemental chemical compositions of melt-spun ribbons and the SPS sample were studied with a FEI Quanta 250 ESEM. The presented images correspond to backscattered electrons (BSE), whereas EDS analyses were performed to study both the elemental chemical composition of localized areas of the samples and for the mapping of Ho and Er. Prior to SEM studies, the SPS composite was mechanically polished and then etched with Nital (10 % nitric acid volumetric) for 10 seconds.

Magnetization measurements were performed using the vibrating sample magnetometer (VSM) option of a 9 T Quantum Design PPMS® Dynacool® system. The measured samples were nearly parallelepiped in shape with the approximate following dimensions of: (*i*) 3 mm (length) × 1.2 mm (width) × 37 μm (thick) for melt-spun ribbons; (*ii*) 3 mm (length) × 1.2 mm (width) × 110 μm (thick) for the so-called mechanical composite which consisted of three ribbon pieces whapped in Kapton tape, and; (*iii*) 3.5 mm (length) × 1 mm (width) × 0.5 mm (thick) for SPS composite bulk alloy. The magnetic field $\mu_o H$ was applied parallel to the longer sample length to reduce the internal demagnetizing field. The thermal dependencies of magnetization, the $M(T)$ curves, were measured at 5 mT and 2 T with a temperature sweep rate of 1.0 K min^{-1} always following a field-cooled regimen. The temperature dependence of the magnetic entropy change $\Delta S_M(T)$ for $\mu_o \Delta H$ values equal or less than 2 T was estimated through the numerical integration of the Maxwell relation (i.e., _____) [2] from a set of isothermal magnetization $M(\mu_o H)$ curves measured on continuous heating in the temperature interval of the magnetic transition. The refrigerant capacity (*RC*), another important MC figure of merit for magnetic refrigeration applications, was estimated: (a) by the product $|\Delta S_M|^{max} \times \delta T_{FWHM}$ (referred to as *RC*-1); (b) by the integral under the $|\Delta S_M(T)|$ curve between T_{hot} and T_{cold}, with $\delta T_{FWHM} = T_{hot} - T_{cold}$ (referred to as *RC*-2); and (c) by the maximum of the product $|\Delta S_M| \times \delta T^{RC\text{-}3}$ under the $\Delta S_M(T)$ curve (referred to as *RC*-3) (for further details see, for instance, Ref. [46]).

3. Results and discussion

3.1 Precursor ribbons characterization and its mechanical composite.

Fig. 1(a) and (b) show SEM micrographs of the typical microstructure at their cross-section of $HoAl_2$ and $ErAl_2$ ribbons, respectively. They were polycrystalline and formed by irregular in shape grains that did not exhibit a visible preferent grain orientation with respect to both ribbon surfaces. The approximate ribbon thickness for both materials was ~ 36 - 40 μm. Room temperature X-ray powder diffractions patterns (Fig. 1(c) and 1(d)) revealed that the samples crystallized in a single phase with the $MgCu_2$-type crystal structure (C15; space group Fd m). From the Le Bail fit of the experimental patterns, we found values for the cell parameter *a* of 7.8109(1) and 7.7 1(1) for o l_2 and $ErAl_2$ ribbon samples, respectively, which are in good in agreement with the data found in literature for bulk alloys of both compounds [47].

The $M(T)$ curves at 5 mT together with the $\Delta S_M(T)$ curves at $\mu_o\Delta H$ = 2 T are plotted in Fig. 2(b). From the minimum of the dM/dT vs. T curves, displayed in Fig. 2(a), we obtained values of Curie temperature for the $HoAl_2$ and $ErAl_2$ ribbon samples of 24 K and 12.5 K, respectively. It is worth mentioning that the T_C measured for the $HoAl_2$ ribbons is below the value reported in the literature [26-27], but notice that the thermomagnetic curve shows a broad major decay followed by a minor knee at 28 K that we attribute to the disorder which is created by the rapid solidification process. On the contrary, the T_C measured for $ErAl_2$ showed a good agreement with the reported for bulk alloys [28-29]. The vertical dashed lines depicted from Fig. 2(a) to (b) serve as a guide for the eyes to underline that the peak value of $\Delta S_M(T)$ for both compounds appears at the respective T_C. Whereas the shape of $\Delta S_M(T)$ and by $|\Delta S_M|^{max}$ at 2 T for $ErAl_2$ agrees with the reported for bulk alloys [22, 28-29], $\Delta S_M(T)$ for $HoAl_2$ broadens leading to $|\Delta S_M|^{max}$ values below those reported for bulk alloys [22, 29]. But the latter is consistent with the widening of the $M(T)$ curve and the observation of two successive magnetic transitions.

The total magnetic entropy change curve $\Delta S_M(T)^{comp}$ for a mechanical biphasic composite based on the synthesized $HoAl_2$ and $ErAl_2$ melt-spun ribbon samples for a magnetic field change of 2 T was obtained. For the latter, it was assumed that it is given by the simple summation of the $\Delta S_M(T)$ curve for the individual compounds multiplied by their corresponding weight fraction value, i.e., μ μ μ . Varying x from 0 to 1, the optimum mixture of these two compounds for $\mu_o\Delta H$ = 2 T was 0.28 ($ErAl_2$) + 0.72 ($HoAl_2$); the resulting $\Delta S_M(T,\ 2\ T)^{comp}$ is shown in Fig. 3. As expected, the nearly flat region appeared between the T_C values of both constituents (i.e., from 12 to 24 K). To experimentally confirm the consistency of this result, we prepared a sample (hereafter referred to as mechanical composite) by wrapping two ribbon pieces with the estimated optimum weight fraction and from the isothermal magnetization curves determined $\Delta S_M(T)^{comp}$. Fig. 3 shows that both curves overlap as a confirmation of the excellent agreement between the calculated and the experimentally measured curves.

3.2 Spark plasma sintering process.

Once that the wrapped ribbons demonstrated a table-like MC behavior at 2 T, then we consolidated the composite through the spark plasma sintering process, which was carried out in a Labox-210 SPS system from Sinter Land Inc.; the sample temperature was measured with a radiation pyrometer focused on the central part

of the external graphite die surface (temperature range: from 600 to 3000°C). Ribbons were weighed in the estimated proportion, homogeneously mixed and introduced into a graphite die of 10.4 mm inner diameter (total mass about 1.0 g). To avoid oxidation, the SPS chamber was purged and filled up with UHP Ar several times before vacuum sealing. A constant pressure of 30 MPa was applied during the SPS process, while the electrical pulsed current was progressively increased in steps of 50 A min^{-1}. The time evolution of both the sample temperature (above 750 ^{o}C) and the vertical displacement of the punches are depicted in Fig. 4. These two parameters provide direct information about thermal expansion and shrinkage of the sample along the process. As shown in the figure, the temperature rises linearly from 600 to 1250 ^{o}C and exponentially decreases after the current is switched off. The sample first undergoes a thermal dilatation upon heating up to ~ 765 ^{o}C and between this temperature and ~ 1080 ^{o}C sintering shrinkage occurs; the estimated sintering time was ~ 2.6 min. The dashed rectangle is a guide to the eyes to indicate the temperature interval and time in which the sintering process takes place. The density ρ calculated for the as-sintered cylindrical in shape sample was 6.0 × 10^3 kg/m^3. From the density values reported for $HoAl_2$ (ρ = 6.085 × 10^3 kg/m^3) [48] and $ErAl_2$ (ρ = 6.208 × 10^3 kg/m^3) [49], we estimated that the as-sintered composite shows a compaction of ~ 97.5 %.

3.3 SPS composite: structural, microstructural and magnetocaloric characterization.

The experimental X-ray powder diffractogram for the composite is shown in Fig. 5. It resembles to that of the individual components. The Bragg reflections of both phases seem not to split since their corresponding lattice parameters are quite close (7.7928(2) and 7.8115(1) for $ErAl_2$ and $HoAl_2$, respectively, agreeing with the lattice parameters of the parental samples); the vertical lines drawn to indicate the position of the diffraction lines, that are visible coincident, also highlight this fact. So, this XRD pattern evidences that the SPS sintered sample shows the $MgCu_2$-type crystal structure.

The as-sintered sample was cut parallel to the pressing direction by using a low-speed diamond saw and the surface of one of the cut pieces was prepared for metallographic observation by a fine polishing followed by etching during a few seconds with Nital to better reveal grain boundaries and any other relevant microstructural feature. A representative SEM image of the characteristic microstructure of the as-sintered sample is shown in Fig. 6a; the vertical dashed line indicates the direction of the pressure applied during sintering. In the sample, we recognize two different regions that can be easily identified by the observed different average grain size. EDS analyses were performed to identify the elemental chemical constitution of

both regions. Fig. 6(b) and (c), show the elemental mapping for Ho and Er, respectively, whereas Fig. 6(d) and (e) the EDS spectrum for each region. Complementing the information provided by both techniques, we conclude that smaller and larger average grain size regions correspond to $HoAl_2$ and $ErAl_2$, respectively. From EDS spectra the 1:2 Laves phase composition (i.e., 33.3:66.6 at.%) was confirmed within the 1.0 at.% experimental error of the determination. In accordance with the high-density value estimated for the sintered sample, the observed porosity is very low whereas the small white regions are attributed to local oxidation due to sample preparation. Thus, the as-sintered composite is basically formed by stacked ribbon flakes whose surfaces tend to be perpendicularly oriented to the pressing direction. The dominant 2D macroscopic shape of ribbons together with the direction of the compressive stress permanently applied during the sintering process favor the formation of this layered-like structure.

Fig. 7 shows the thermomagnetic $M(T)$ curves at 5 mT and 2 T; the $dM/dT(T)$ curve at 5 mT appears at the inset to highlight the observed magnetic transitions. In the $M(T)$ curve at 5 mT two transitions are detected: one revealed by the slight knee that appears around 12 K that comes from the minor fraction of $ErAl_2$ [28-29], and a subsequent major one around 25 K that is close to the T_C of $HoAl_2$ as-cast ribbons. It is worth to note that the latter transition is more abrupt than the phase transition shown by $HoAl_2$ ribbons, which suggests an enhancement of the structural order associated with the thermal processing. As shown in the figure, the SPS composite exhibits a smooth and broad decay of its saturation magnetization at 2 T.

Fig. 8(a) shows the isothermal magnetization curves measured up to 2 T, whereas Fig. 8(b) shows the resulting $\Delta S_M(T)^{comp}$ at $\mu_o \Delta H$ = 2 T for the as-sintered composite compared with the curve computed for the two-ribbons mechanical composite plotted in Fig. 3; $|\Delta S_M|^{max}$ reaches a value of 12.1 J kg^{-1} K^{-1}, but its average value over the flattened region is 10.6 J kg^{-1} K^{-1}. Despite of the discrepancy observed around the magnetic transition temperature of $HoAl_2$ (that as previously shown is shifted to a lower temperature with respect to the reported for this compound in bulk form), the agreement between both curves is quite good. In fact, a nearly constant region in $\Delta S_M(T)^{comp}$ appears between 11 and 26 K. There are two factors that play a positive role in the obtained result: (a) according to the respective binary R-Al phase diagrams [50-51], the two compounds that form the biphasic composite are line compounds. This means that they will not decompose during the SPS process; (b) diffusion during sintering appears in two regions: the grains that form the ribbons of $HoAl_2$ or $ErAl_2$, and the interface between neighboring ribbon pieces that can be either of the same or two different

compounds. The diffusion during sintering inside a ribbon piece of one of the two RAl_2 compounds will only lead to increase the average grain size of that phase. However, the diffusion across interface between ribbons of the two different compounds will tend to form a solid solution of the type $R_{1-x}R'_xAl_2$. But the width of the interfacial region is negligible with respect to the macroscopic dimensions of the ribbons pieces (as shown, for instance, in Ref. [44]). Thus, the volumetric fraction of the interfacial regions between $HoAl_2$ and $ErAl_2$ in which a solid solution would be formed could also be negligible in comparison with the volume fraction of phases $HoAl_2$ and $ErAl_2$ that form the resulting SPS composite.

Table 1 summarizes the magnetocaloric properties of the precursor ribbons, mechanical composite, and SPS composite derived from the respective $\Delta S_M(T)$ curves at $\mu_o\Delta H$ = 2 T. In addition, Fig. 8(c) shows the magnetic field change dependence of the refrigerant capacity *RC* estimated according to the following criteria [1, 52]: (a) *RC*-1, from the product $|\Delta S_M|^{max} \times \delta T_{FWHM}$, where δT_{FWHM} is the temperature interval corresponding to the full-width at half-maximum of the $\Delta S_M(T)$ curve (i.e., $\delta T_{FWHM} = T_{hot} - T_{cold}$; usually assumed as the working temperature span of the thermodynamic cycle); (b) *RC*-2, by calculating the area below the $\Delta S_M(T)$ for the interval δT_{FWHM}, and; (c) *RC*-3, by maximizing the product $\Delta S_M \times \delta T$ below the $\Delta S_M(T)$ curve (Wood and Potter criterion). In addition, the inset in Fig. 8(c) displays the evolution of T_{hot} and T_{cold} with $\mu_o\Delta H$; notice that the composite shows a well-defined δT_{FWHM} for $\mu_o\Delta H$ above 0.38 (i.e., after the $\Delta S_M(T)$ curves of both components becomes broader enough with the $\mu_o\Delta H$ increase to progressively draw the table-like trend). The observed increment in *RC*-1 and *RC*-2 for the SPS and mechanical composites compared to the respective values for the precursors (see the Table) result from the $\Delta S_M(T)$ broadening; δT_{FWHM} for the mechanical and SPS composites is about 2.5 and 0.5 times larger than that shown by $ErAl_2$ and $HoAl_2$ precursors, respectively. For *RC*-3, the table-like shape of the $\Delta S_M(T)$ curve explains the greater value shown by the composites; the reduction of $|\Delta S_M|$ at $T=T_{hot}$ (or equivalently, T_{cold}) compared to $|\Delta S_M|^{max}$ is about 20 % for the composites, whereas it is close to 45 % and 60 % for $HoAl_2$ and $ErAl_2$ precursors, respectively. In fact, restricting the temperature range to the table-like zone (i.e., between 12 and 25 K), the effective *RC*, defined as $RC_{eff}= |\Delta S_M(T_C^A) \times (T_C^A - T_C^B)|$ [16], for the composites results to be ~130 J kg^{-1}. The larger refrigerant capacity of the SPS composite arises from its greater δT_{FWHM}. At last, the large refrigerant capacity of the SPS composite compared with the reported for individual compounds in a similar temperature range is highlighted. Focusing,

compounds. The diffusion during sintering inside a ribbon piece of one of the two RAl_2 compounds will only lead to increase the average grain size of that phase. However, the diffusion across interface between ribbons of the two different compounds will tend to form a solid solution of the type $R_{1-x}R'_xAl_2$. But the width of the

for instance, on the *RC*-1 value at 2 T it must be noticed that it is not only comparable but larger than the

reported in earlier studies for single rare earth-based compounds able to work in a similar temperature range referred as good magnetic refrigerants such as DyCoAl (234 J kg^{-1}), $DyNi_2$ (140 J kg^{-1}), DyCuAl (190 J kg^{-1}), and $ErNi_3$ (173 J kg^{-1}) [53-56].

4. Conclusions.

In conclusion, in this work we have demonstrated the potential of the SPS technique to fabricate highly-dense two-phase MC composites by using rapidly solidified melt-spun ribbons as starting components, a geometry particularly advantageous since the formation of mixed regions of the two components by diffusion is limited to the interface between them, whose volume fraction is negligible with respect to the total volume of the two phases (that remains dominant). This was exemplified with the synthesis of a two-phase MC composite based on the magnetocaloric Laves phases RAl_2 with R= Ho and Er. The proportion of both precursors was analyzed to obtain a table-like $\Delta S_M(T)^{comp}$ curve in the cryogenic temperature range. Such a table-like shaped $\Delta S_M(T)$ curve is a prerequisite for developing magnetic refrigerants for their use as working bodies for magnetic refrigeration devices working on the Ericsson-like refrigeration cycle. For a magnetic field change of 2 T, the designed composite, whose composition was 28 wt.% ($ErAl_2$) + 72 wt.% ($HoAl_2$), showed a nearly flat $\Delta S_M^{comp}(T)$ curve in the temperature range 11 K - 26 K with an average $|\Delta S_M|^{max}$ value of 10.6 J kg^{-1} K^{-1}, δT_{FWHM} $\approx$ 25 K and an enhanced refrigerant capacity with respect to the precursors. Looking forward, we hope these results could become a source of inspiration for using the SPS technique to develop magnetocaloric composites with a conveniently designed magnetocaloric effect curve in different temperature ranges which could be used in magnetic refrigeration devices.

Declaration of competing interest

The authors declare that they have no known competing financial interests or personal relationships could have appeared to influence the work reported in this paper.

Credit authorship contribution statement

J.L. Sánchez Llamazares: Conception or design of the work, methodology, data collection, data analysis and

reported in earlier studies for single rare earth-based compounds able to work in a similar temperature range referred as good magnetic refrigerants such as DyCoAl (234 J kg^{-1}), $DyNi_2$ (140 J kg^{-1}), DyCuAl (190 J kg^{-1}), and $ErNi_3$ (173 J kg^{-1}) [53-56].

Interpretation, writing and final draft; Final approval of the version to be published. **J. Zamora**: Data collection,

data analysis and interpretation, article initial drafting. **C.F. Sánchez-Valdés**: Data collection, data analysis and interpretation, Software, Critical revision of the article. **P. Álvarez Alonso**: Conception or design of the work, Data collection, data analysis and interpretation, Software, Final approval of the version to be published. All authors read and approved the final manuscript.

Acknowledgements. The support received from the following organizations is gratefully acknowledged: (a) Laboratorio Nacional de Nanociencias y Nanotecnología (LINAN, IPICyT); (b) Consejo Potosino de Ciencia y Tecnología (Copocyt); (c) Banco Santander Central Hispano; (d) Spanish MCIU and AEI and European FEDER (MCIU-19-RTI2018- 094683-B-C52), and; (e) Principado de Asturias (IDI/2018/000185), Spain. Authors are also indebted to M.Sc. B.A. Rivera-Escoto, M.Sc. A.I. Peña Maldonado, and Dr. G.J. Labrada-Delgado (from LINAN) and D. Martínez Blanco (from scientific and technological resources of the University of Oviedo) for the technical support given. J. Zamora thanks to CONACyT-México for supporting his postdoctoral position at IPICYT. C.F. Sánchez-Valdés is grateful to DMCU-UACJ for supporting his research stays at IPICyT (program PFCE and academic mobility grant); also, for the financial support received from SEP-Conacyt, Mexico (Grant No. A1-S-37066).

References

[1] A. M. Tishin, Y. I. Spichkin, **The Magnetocaloric Effect and its Applications**, Institute of Physics Publishing, Bristol, 2003.

[2] K.A. Gschneidner Jr, V.K. Pecharsky, **Magnetic refrigeration materials (invited)**, J. Appl. Phys. 85 (1999) 5365-5368.

[3] B.J. Korte, V.K. Pecharsky, K. A. Gschneidner Jr., **The correlation of the magnetic properties and the magnetocaloric effect in $(Gd_{1-x}Er_x)NiAl$ alloys**, J. Appl. Phys. 84 (1998) 5677.

[4] H. Wada, Y. Tanabe, K. Hagiwara, M. Shiga, **Magnetic phase transition and magnetocaloric effect of $DyMn_2Ge_2$**, J. Magn. Magn. Mater 218 (2000) 203-210.

[5] H. Fu, Z. Ma, X.J. Zhang, D.H. Wang, H. Teng, E. Agurgo Balfour, **Table-like magnetocaloric effect in the Gd-Co-Al alloys with multi-phase structure**, Appl. Phys. Lett. 104 (2014) 072401.

[6] . . aw, . . oreno- am rez, J.S. Blazquez, V. Franco, A. Conde, **G+GdZn biphasic magnetic composites synthesized in a single preparation step: Increasing refrigerant capacity without decreasing magnetic entropy change**, J. Alloys Compd. 675 (2016) 244-247.

[7] X.Y. Shen, X.C. Zhong, X.W. Huang, H.Y. Mo, X.L. Feng, Z.W. Liu, D.L. Jiao, **Achieving a table-like magnetocaloric effect and large refrigerant capacity in in situ multiphase $Gd_{65}Mn_{25}Si_{10}$ alloys obtained by crystallization treatment**, J. Phys. D: Appl. Phys. 50 (2017) 035005.

[8] L. Li, C. Xu, Y. Yuan, S. Zhou, **Large refrigerant capacity induced by table-like magnetocaloric effect in amorphous $Er_{0.2}Gd_{0.2}Ho_{0.2}Co_{0.2}Cu_{0.2}$ ribbons**, Mater. Res. Lett. 6 (2018) 413-418.

[9] T. Hashimoto, T. Kuzuhara, M. Sahashi, K. Inomata, A. Tomokiyo, H. Yayama, **New application of complex magnetic materials to the magnetic refrigerant in an Ericsson magnetic refrigerator**, J. Appl. Phys. 62 (1987) 3873-3878.

[10] T. Hashimoto, T. Kuzuhara, K. Matsumoto, M. Sahashi, K. Imonata, A. Tomokiyo, H. Yayama, **A new method of producing the magnetic refrigerant suitable for the Ericsson magnetic refrigeration**, IEEE Trans. Magn. 23 (1987) 2847-2849.

[11] A. Chaturvedi, S. Stefanoski, M.-H. Phan, G.S. Nolas, H. Srikanth, **Table-like magnetocaloric effect and enhanced refrigerant capacity in $Eu_8Ga_{16}Ge_{30}$-EuO composite materials**, Appl. Phys. Lett. 99 (2011) 162513.

[12] P. Álvarez, J.L. Sánchez Llamazares, P. Gorria, J.A. Blanco, **Enhanced refrigerant capacity and magnetic entropy flattening using a two-amorphous FeZrB(Cu) composite**, Appl. Phys. Lett. 99 (2011) 232501.

[13] . . barra- ayt n, . . nchez lamazares, P. lvarez- lonso, . . nchez- ald s, P. Gorria, J.A. Blanco, **Magnetic entropy table-like shape in RNi_2 composites for cryogenic refrigeration**, J. Appl. Phys. 117 (2015) 17C116.

[14] R. Caballero-Flores, V. Franco, A. Conde, K.E. Knipling, M.A. Willard, **Optimization of the refrigerant capacity in multiphase magnetocaloric materials**, Appl. Phys. Lett. 98 (2011) 102505.

[15] A. Smaïli, R. Chahine, **Composite materials for Ericsson-like magnetic refrigeration cycle**, J. Appl. Phys. 81 (1997) 824-829.

[16] P. Álvarez, P. Gorria, J.L. Sánchez Llamazares, J.A. Blanco, **Searching the conditions for a table-like shape of the magnetic entropy in magnetocaloric materials**, J. Alloys Compd. 568 (2013) 98-101.

[17] H. Zhang, R. Gimaev, B. Kovalev, K. Kamilov, V. Zverev, A. Tishin, **Review on the materials and devices for magnetic refrigeration in the temperature range of nitrogen and hydrogen liquefaction**, Phys. B: Cond. Matter. 558 (2019) 65-73.

[18] K.A. Gschneidner Jr., V.K. Pecharsky, **Magnetocaloric materials,** Annu. Rev. Mater. Sci. 30 (2000) 387-429.

[19] V.K. Pecharsky, K.A. Gschneidner Jr., S. Yu. Dan´kov, A.M. Tishin, **Magnetocaloric Properties of Gd_3Al_2**, Cryocoolers 10 (1999) 639-645.

[20] S. Yu. Dan´kov, V.V. Ivtchenko, A.M. Tishin, K.A. Gschneidner Jr., V.K. Pecharsky, **Magnetocaloric Effect in $GdAl_2$ and Nd_2Fe_{17}**, Adv. Cryogenic Engin. Mater. 46 (2000) 397-404.

[21] S.A. Nikitin, A.M. Tishin, **Magnetocaloric effect in $HoCo_2$ compound**, Cryogenics 31 (1991) 166-167.

[22] N.A. de Oliveira, P.J. von Ranke, **Theoretical aspects of the magnetocaloric effect**, Phys. Reports 489 (2010) 89-159.

[23] K.A. Gschneidner, Jr., V.K. Pecharsky, **Binary rare earth Laves phases - an overview**, Zeitschrift Für Krist. - Cryst. Mater. 221 (2006) 375-381.

[24] W. Schelp, A. Leson, W. Drewes, H.-G. Purwins, H. Grimm, **Magnetization and magnetic excitations in $HoAl_2$**, Z. Physik B- Cond. Matter 51 (1983) 41-47.

[25] H. Oesterreicher, **Structural and Magnetic Studies on $ErFe_2$-$ErAl_2$**, J. Appl. Phys. 42 (1971) 5137-5143.

[26] T. Hashimoto, K. Matsumoto, T. Kurihara, T. Numazawa, A. Tomokiyo, H. Yayama, T. Goto, T. Todo, M. Sahashi, **Investigations on the possibility of the RAl_2 system as a refrigerant in an Ericsson type magnetic refrigerator**, Adv. Cryog. Eng. 32 (1986) 279-286.

[27] L.A. Gil, J.C.P. Campoy, E.J.R. Plaza, M.V.de Souza, **Conventional and anisotropic magnetic entropy change in $HoAl_2$ ferromagnetic compound**, J. Magn. Magn. Mater. 409 (2016) 45-49.

[28] K.A. Gschneidner Jr, V.K. Pecharsky, **The $(Dy_{1-x}Er_x)Al_2$ alloys as active magnetic regenerators for magnetic refrigeration**, Adv. Cryog. Eng. 42 (1996) 475-483.

[29] J.C.P. Campoy, E. J. R. Plaza, A. A. Coelho, S. Gama, **Magnetoresistivity as a probe to the field-induced change of magnetic entropy in RAl_2 compounds R= Pr, Nd, Tb, Dy, Ho, Er**, Phys. Rev. B 74 (2006) 134410.

[30] M. Khan, K.A. Gschneidner Jr., V.K. Pecharsky, **Spin reorientation transitions in $Ho_{1-x}Dy_xAl_2$ alloys**, J. Appl. Phys. 110 (2011) 103912.

[31] P.J. von Ranke, V.K. Pecharsky, K.A. Gschneidner Jr., **Influence of the crystalline electrical field on the magnetocaloric effect of $DyAl_2$, $ErAl_2$, and $DyNi_2$**, Phys. Rev. B 58 (1998) 12110.

[32] A.L. Lima, K.A. Gschneidner Jr., V.K. Pecharsky, A.O. Pecharsky, **Disappearance and reappearance of magnetic ordering upon lanthanide substitution in $(Er_{1-x}Dy_x)Al_2$**, Phys. Rev. B 68 (2003) 134409.

[33] P. Cavaliere, B. Sadeghi, A. Shabani, **Spark Plasma Sintering: Process Fundamentals**, in: Spark Plasma Sinter. Mater., Springer International Publishing, Cham, 2019: pp. 3–20.

[34] M. Suárez, A. Fernández, J.L. Menéndez, R. Torrecillas, H.U. Kessel, J. Hennicke, R. Kirchner, T. Kessel, **Challenges and Opportunities for Spark Plasma Sintering: A Key Technology for a New Generation of Materials**, in: Sinter. Appl., InTech, 2013. DOI: 10.5772/53706.

[35] A.T. Saito, T. Hirakawa, S. Kaji, **Development of Synthesis Process of Magnetocaloric Material of La(Fe, Co, Si)$_{13}$** Int. J. Eng. Innov. Res. 4 (2015) 803-809.

[36] A. Patissier, V. Paul-Boncour, **Fast synthesis of $LaFe_{13-x}Si_x$ magnetocaloric compounds by reactive Spark Plasma Sintering**, J. Alloys Compd. 645 (2015) 143-150.

[37] P. Shamba, N. A. Morley, O. Cespedes, I. M. Reaney, W. M. Rainforth, **Optimization of magnetocaloric properties of arc-melted and spark plasma-sintered $LaFe_{11.6}Si_{1.4}$**, Appl. Phys. A 122 (2016) 732.

[38] W.B. Fan, Y.H. Hou, X.J. Ge, Y.L. Huang, J.M. Luo, Z.C. Zhong, **Microstructure and improved magnetocaloric properties: LaFeSi/LaAl magnets prepared by spark plasma sintering technique**, J. Phys. D: Appl. Phys. 51 (2018) 115003.

[39] M. Yue, M.F. Xu, H.G. Zhang, D.T. Zhang, D.M. Liu, Z. Altounian, **Structural and magnetocaloric properties of $MnFeP_{1-x}Si_x$ compounds prepared by spark plasma sintering**, IEEE Trans. Magn. 51 (2015) 2504804.

[40] D.M. Liu, H. Zhang, S.B. Wang, W.Q. Xiao, Z.L. Zhang, N. Tian, C.X. Liu, M. Yue, Q.Z. Huang, J.X. Zhang, J.W. Lynn, **The effect of Al doping on the crystal structure and magnetocaloric behavior of $Mn_{1.2}Fe_{0.8}P_{1-x}Ge_x$ compounds**, J. Alloys Compd. 633 (2015) 120-126.

[41] Z.R. Zhao, T. Jing, G.F. Wang, B.Y. Yang, X.F. Zhang, **Influences of sintering temperature on the microstructure and magnetocaloric effect of $Mn_{1.15}Fe_{0.85}P_{0.65}Si_{0.13}Ge_{0.2}B_{0.02}$ prepared by spark plasma sintering**, IEEE International Magnetics Conference (INTERMAG) 1800006 (2018) 1-5 (DOI: 10.1109/INTMAG.2018.8508728).

[42] G. F. Wang, B. Y. Yang, T. Jing, Z. R. Zhao, X. F. Zhang, Y. L. Liu, **A comparative study of the magnetocaloric effect in MnFePSiGeB prepared by traditional sintering and spark plasma sintering**, IEEE Trans. Magn. 55 (2019) 2500705.

[43] H. Imam, H.G. Zhang, J. Chen, M. Yue, Q.M. Lu, D.T. Zhang, W.Q. Liu, **Powdering and SPS sintering effect on the magnetocaloric properties of MnNiSi-based compound**s, AIP Adv. 9 (2019) 035205.

[44] M. Yue, J. Zhang, H. Zeng, H. Chen, X.B. Liu, **Magnetocaloric effect in $Gd_5Si_2Ge_2$/Gd composite materials**, J. Appl. Phys. 99 (2006) 08Q104.

[45] J. Rodriguez Carvajal, **Recent advances in magnetic structure determination by neutron powder diffraction**, Physica B 192 (1993) 55-69.

[46] P. Gorria, J.L. Sánchez Llamazares, P. Álvarez, M.J. Pérez, J. Sánchez Marcos, J.A. Blanco, **Relative cooling power enhancement in magneto-caloric nanostructured Pr_2Fe_{17}**", . hys D: ppl. hys. 1 (2008) 192003.

[47] ICDD (2016)."Powder Diffraction File," International Centre for Diffraction Data, edited by S. Kabekkodu, 12 Campus Boulevard, Newton Square, Pennsylvania 19073-3272.

[48] I.R. Harris, R.C. Mansey, G.V. Raynor, **Rare earth intermediate phases: III. The cubic laves phases formed with aluminium and cobalt**, J. Less Common Met. 9 (1965) 270-280.

[49] E. Godet, M. Walker, **Magnetoelastic effects on the elastic constants of $HoAl_2$**, Helv. Phys. Acta. 51 (1978) 178-181.

[50] K.A. Gschneidner Jr., F.W. Calderwood, **The Al−Er (Aluminum-Erbium) system,** Bulletin of Alloy Phase Diagrams 9 (1988) 676-678.

[51] K.A. Gschneidner Jr., F.W. Calderwood, **The Al−Ho (Aluminum-Holmium) system**, Bulletin of Alloy Phase Diagrams 9 (1988) 684-686.

[52] P. Gorria, J.L. Sánchez Llamazares, P. Álvarez, M.J. Pérez, J. Sánchez Marcos, J.A. Blanco, **Relative cooling power enhancement in magneto-caloric nanostructured Pr_2Fe_{17}**, J. Phys D: Appl. Phys. **41** (2008) 192003.

[53] X.X. Zhang, F.W. Wang, G.H. Wen, **Magnetic entropy change in RCoAl (R = Gd, Tb, Dy, and Ho) compounds: candidate materials for providing magnetic refrigeration in the temperature range 10 K to 100 K**, J. Phys.: Condens. Matter. **13** (2001) L747.

[54] P.J. von Ranke, V.K. Pecharsky, K.A. Gschneidner Jr**, Influence of the crystalline electrical field on the magnetocaloric effect of $DyAl_2$, $ErAl_2$, and $DyNi_2$**, Phys. Rev. B 58 (1998) 12110.

[55] Q. Y. Dong, B. G. Shen, J. Chen, J. Shen, and J. R. Sun, **Large reversible magnetocaloric effect in DyCuAl compound**, J. Appl. Phys. 105 (2009) 113902.

[56] Q.Y. Dong, J. Chen, J. Shen, J.R. Sun, B.G. Shen, **Magnetic properties and magnetocaloric effects in R_3Ni_2 (R = Ho and Er) compounds,** Appl. Phys. Lett. 99 (2011) 132504.

FIGURE CAPTIONS

Fig. 1. Cross-sectional SEM micrograph and experimental and calculated X-ray powder diffraction patterns for $HoAl_2$ [(a) and (d)] and $ErAl_2$ [(b) and (c)] melt-spun ribbons. XRD patterns were correctly indexed based on the $MgCu_2$-type crystal structure. Vertical green bars in (c) and (d) stand for the Bragg positions of the corresponding pattern, whereas the difference between the observed (solid red circles) and calculated (black line) patterns is depicted by the blue line in the bottom of each graph.

Fig. 2. dM/dT(T) curves (a) and M(T) at 5 mT and $\Delta S_M(T)$ curves for a magnetic field change $\mu_0 \Delta H$ = 2 T (b) for the $HoAl_2$ and $ErAl_2$ precursor ribbons.

Fig. 3. Calculated (open squares) $-\Delta S_M(T)^{comp}$ curve for a magnetic field change of 2 T for the 28 wt.% ($ErAl_2$) + 72 wt.% ($HoAl_2$) composite compared with the one measured (full circles) for the mechanical biphasic composite.

Fig. 4. Evolution of the vertical displacement and temperature with time during the SPS process of the 28 wt.% ($ErAl_2$) + 72 wt.% ($HoAl_2$) composite ribbons. Dashed rectangle and horizontal lines serve as guides to the eyes to indicate the temperature interval and time in which the sintering process occurs.

Fig. 5. X-ray powder diffraction pattern for the as-sintered 28 wt.% ($ErAl_2$) + 72 wt.% ($HoAl_2$) composite. Top and bottom vertical bars indicate the position of Bragg diffraction lines for $ErAl_2$ and $HoAl_2$ compounds, respectively. Vertical green bars in the pattern stand for the Bragg positions of the XRD patterns for individual $ErAl_2$ and $HoAl_2$ compounds, whereas the difference between the measured (solid red circles) and calculated (black line) patterns is depicted by the blue line in the bottom of the graph.

Fig. 6. (a) SEM micrograph of the typical microstructure shown by the as-sintered 28 wt.% ($ErAl_2$) + 72 wt.% ($HoAl_2$) composite. The vertical dashed line indicates the pressing direction during sintering. (b) and (c) images show the elemental mapping for Ho and Er, whereas (d) and (e) show the EDS spectrum taken in the regions indicated as $HoAl_2$ and $ErAl_2$ in the image (a).

Fig. 7. M(T) measured at 5 mT (open red circles) and 2 T (open blue circles) for the as-sintered 28 wt.% ($ErAl_2$) + 72 wt.% ($HoAl_2$) composite. Arrows indicate the magnetization axis that corresponds to each curve. Inset: dM/dT vs T curves for the M(T) curve at 5 mT.

Fig. 8. (a) Isothermal magnetization curves measured in the temperature range 4-50 K for the as-sintered composite. (b) Comparison of $-\Delta S_M(T)^{comp}$ curves for a magnetic field change of 2 T for the calculated (open squares) and as-sintered (full circles) 28 wt.% ($ErAl_2$) + 72 wt.% ($HoAl_2$) composite. (c) Magnetic field change

dependence of the refrigerant capacity *RC* determined from different criteria (see the text for definition), and the temperatures T_{cold} and T_{hot} that define δT_{FWHM} of the $-\Delta S_M(T)^{comp}$ curve (inset) for the as-sintered composite.

TABLE CAPTION

Table 1. Magnetocaloric properties for a magnetic field change of 2 T for $ErAl_2$ and $HoAl_2$ melt-spun precursor ribbons, and the numerically calculated (referred to as mechanical composite) and SPS 28 wt.% ($ErAl_2$) + 72 wt.% ($HoAl_2$) composite.

TABLE

Table 1.

Alloy	SPS bulk composite	Mechanical composite	$ErAl_2$ aq-ribbons	$HoAl_2$ aq-ribbons
$\|\Delta S_M\|^{max}$ (J kg^{-1} K^{-1})	10.6*	10.9*	22.6	11.7
RC-1 (J kg^{-1})	303	279	214	258
RC-2 (J kg^{-1})	244	234	166	203
δT_{FWHM} (K)	25	26	10	22
T_{hot} (K)	33	34	19	35
T_{cold} (K)	8	8	9	13
RC-3 (J kg^{-1})	165	156	109	129
δT^{RC-3} (K)	20	19	12	20
T_{hot} (K) **	30	29	20	34
T_{cold} (K) **	10	10	8	14

* Average value over the flattened temperature interval. ** Related to *RC*-3.

FIGURES

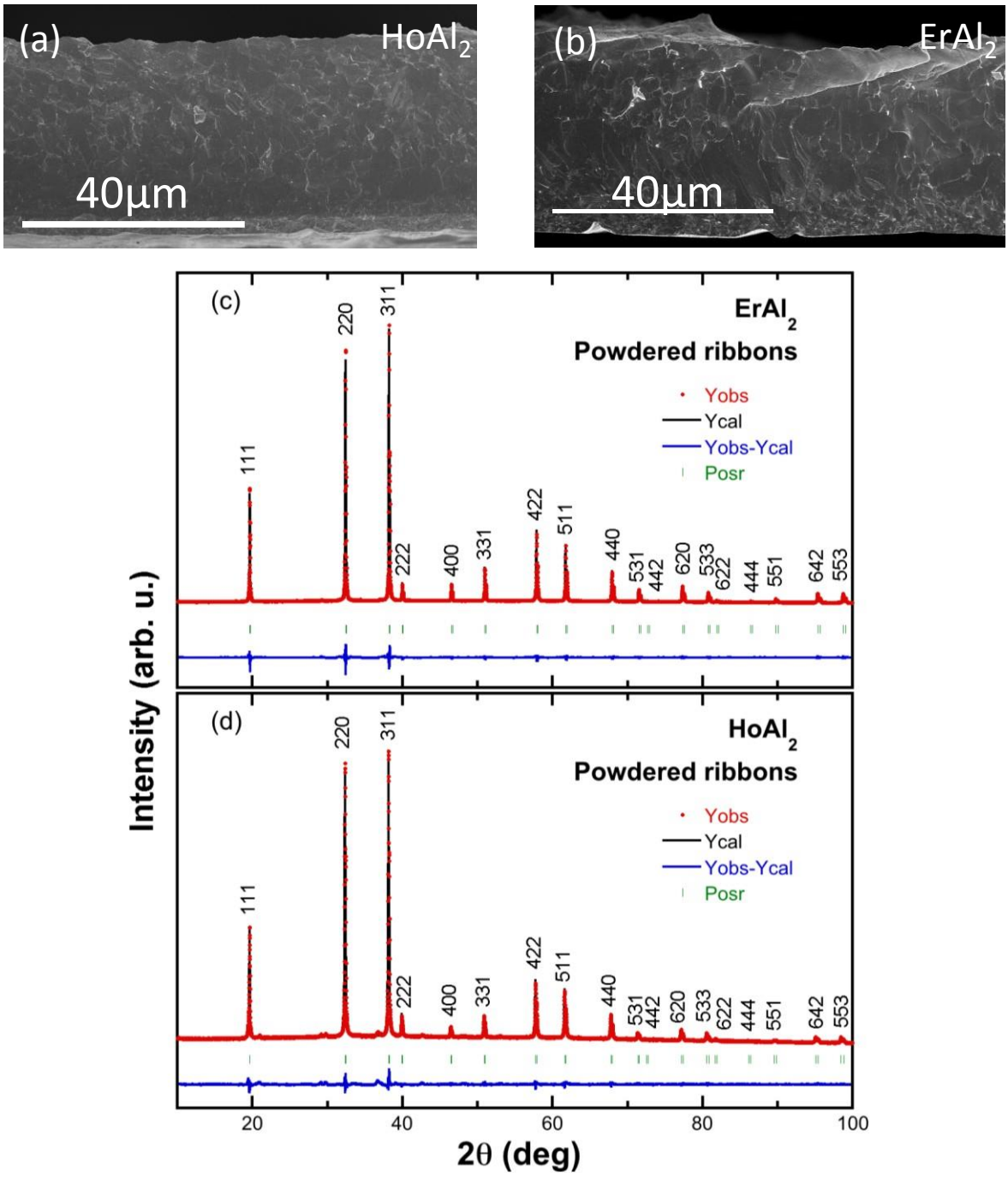

Fig. 1.

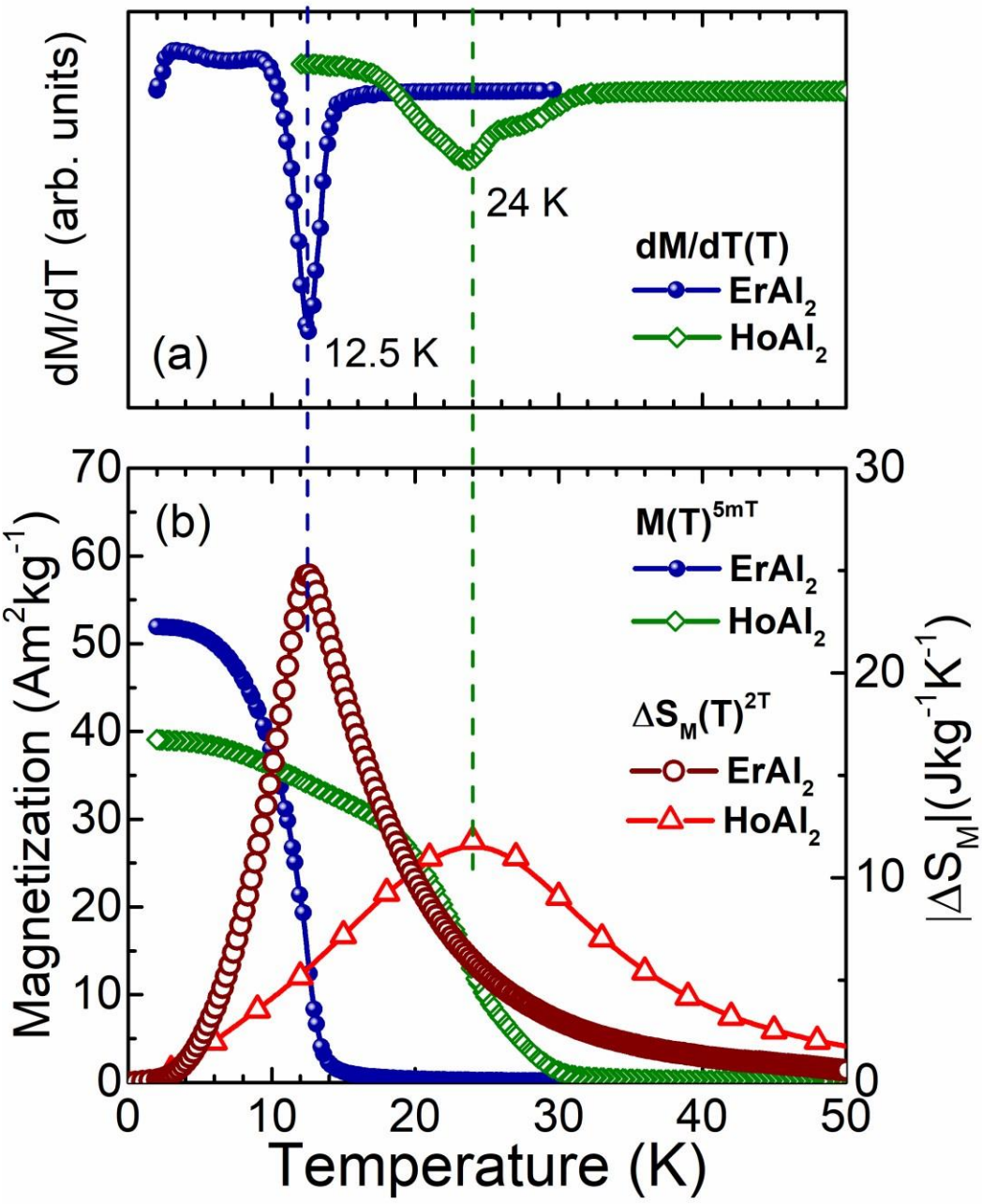
dM/dT (arb. units)
(a)
12.5 K
24 K
dM/dT(T)
ErAl2
HoAl2
(b)
M(T)5mT
ErAl2
HoAl2
ΔSM(T)2T
ErAl2
HoAl2
Magnetization (Am2kg-1)
|ΔSM|(Jkg-1K-1)
Temperature (K)
0
10
20
30
40
50
60
70

Fig. 2.

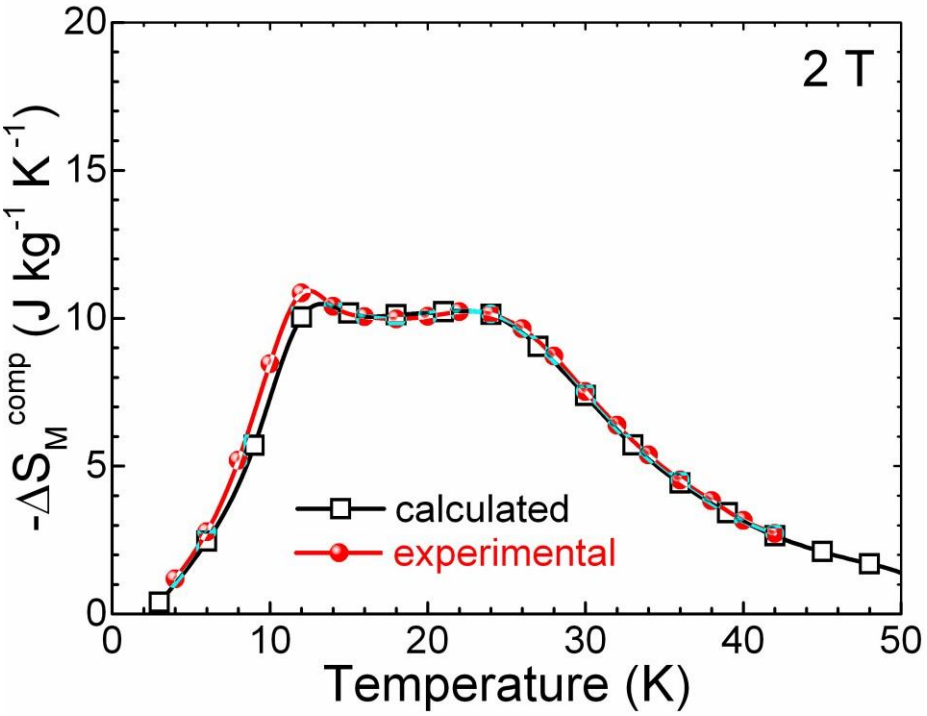
2 T
$-\Delta S_M^{comp}$ (J kg^{-1} K^{-1})
Temperature (K)
calculated
experimental
0
5
10
15
20
0
10
20
30
40
50

Fig. 3.

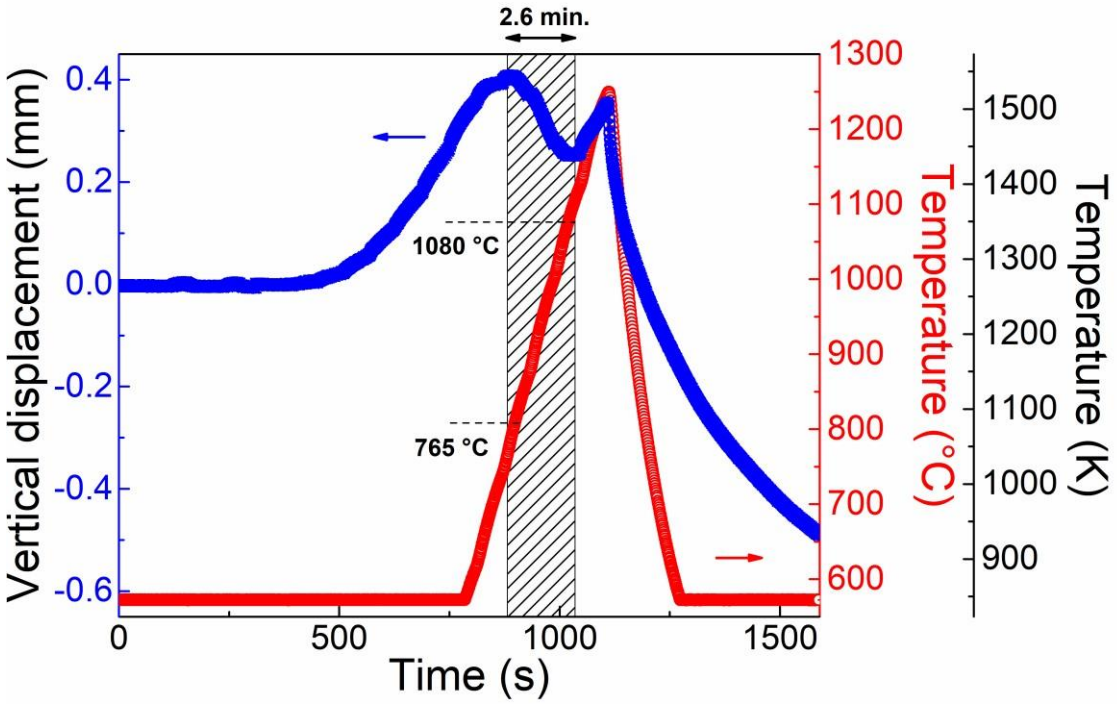
2.6 min.
Vertical displacement (mm)
0.4
0.2
0.0
-0.2
-0.4
-0.6
1080 °C
765 °C
0
500
1000
1500
Time (s)
1300
1200
1100
1000
900
800
700
600
Temperature (°C)
1500
1400
1300
1200
1100
1000
900
Temperature (K)

Fig. 4.

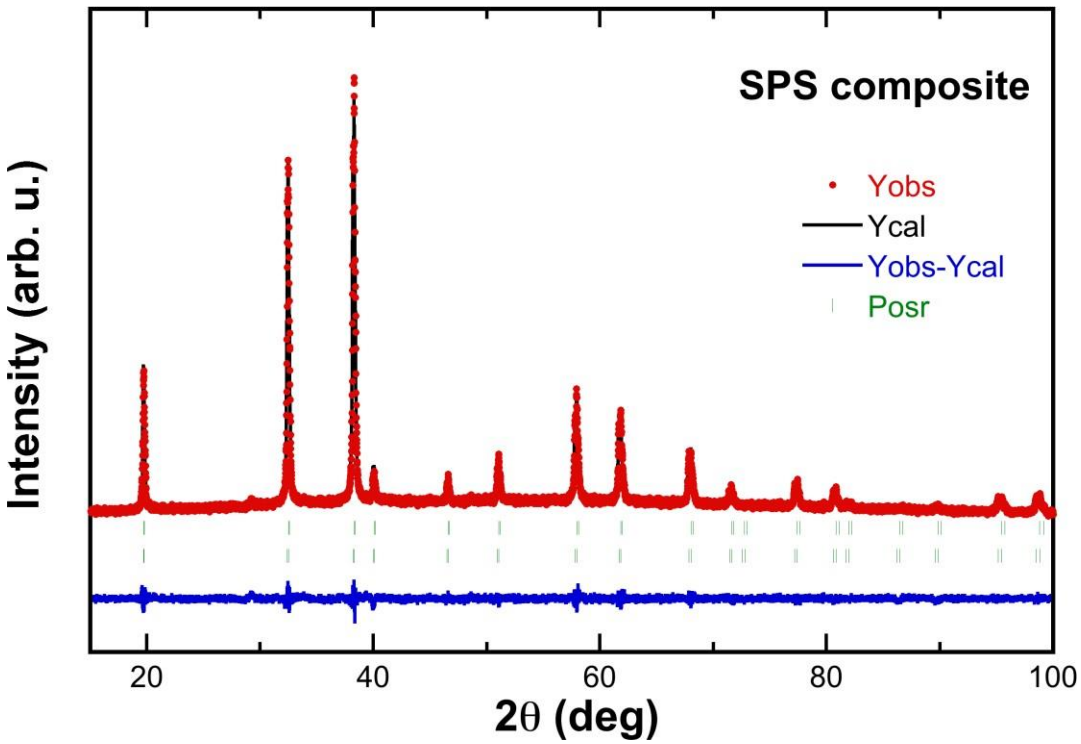
SPS composite
Yobs
Ycal
Yobs-Ycal
Posr
Intensity (arb. u.)
20
40
60
80
100
2θ (deg)

Fig. 5.

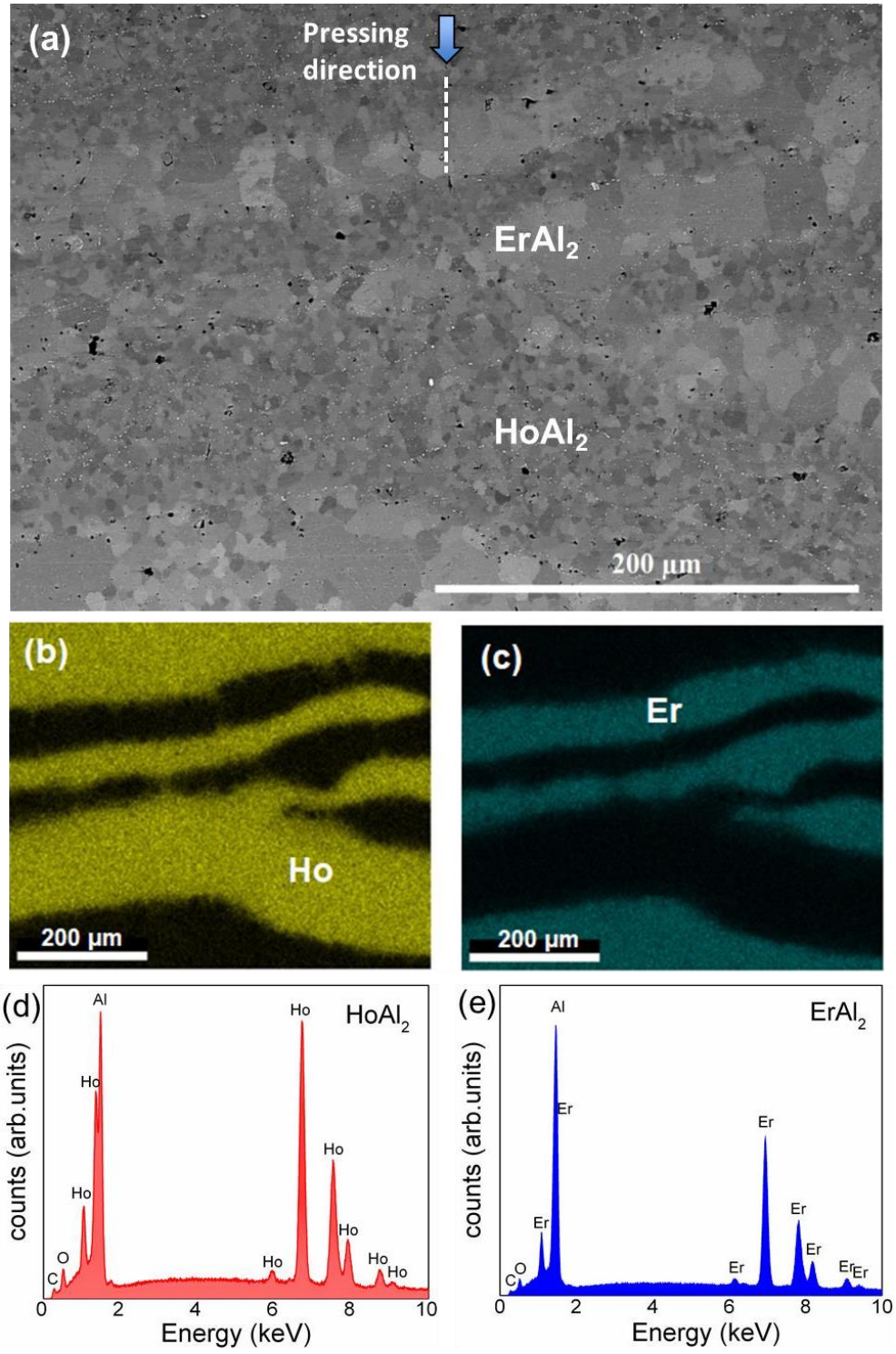
(a)
Pressing direction
ErAl2
HoAl2
200 µm
(b)
Ho
200 µm
(c)
Er
200 µm
(d)
HoAl2
counts (arb.units)
Energy (keV)
Al
Ho
O
C
(e)
ErAl2
counts (arb.units)
Energy (keV)
Al
Er
O
C

Fig. 6.

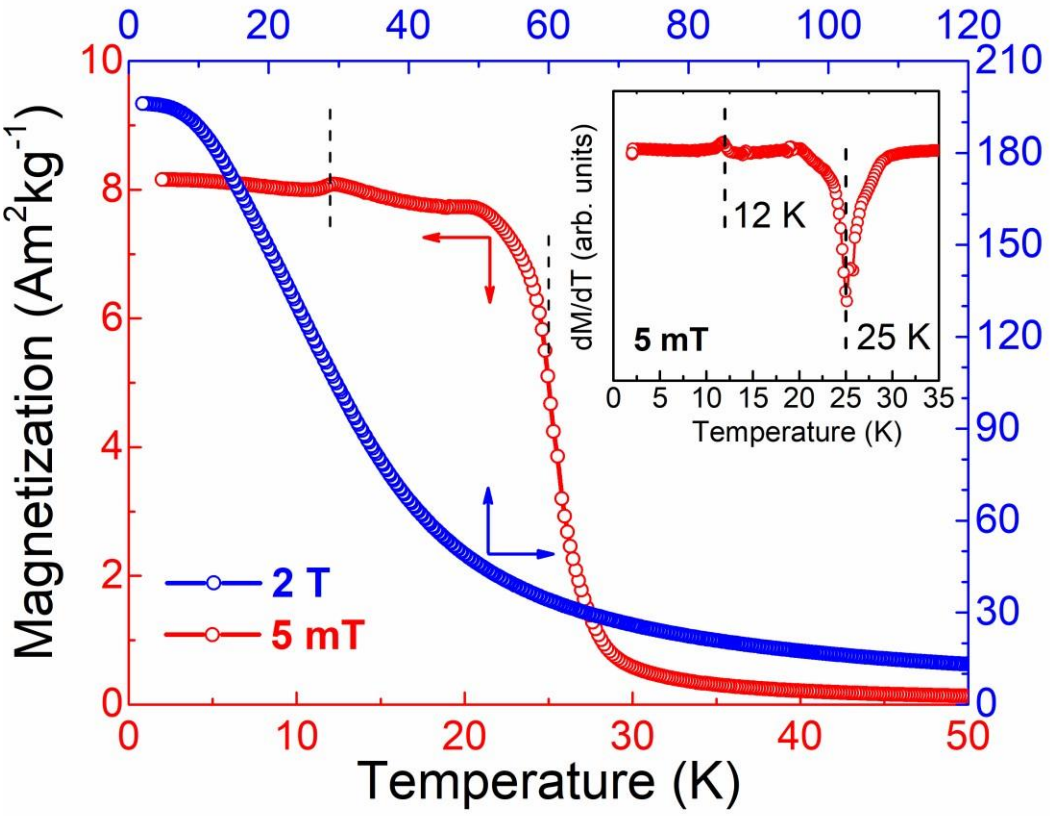
Magnetization (Am^{2}kg^{-1})
Temperature (K)
dM/dT (arb. units)
2 T
5 mT
12 K
25 K
5 mT
Temperature (K)

Fig. 7.

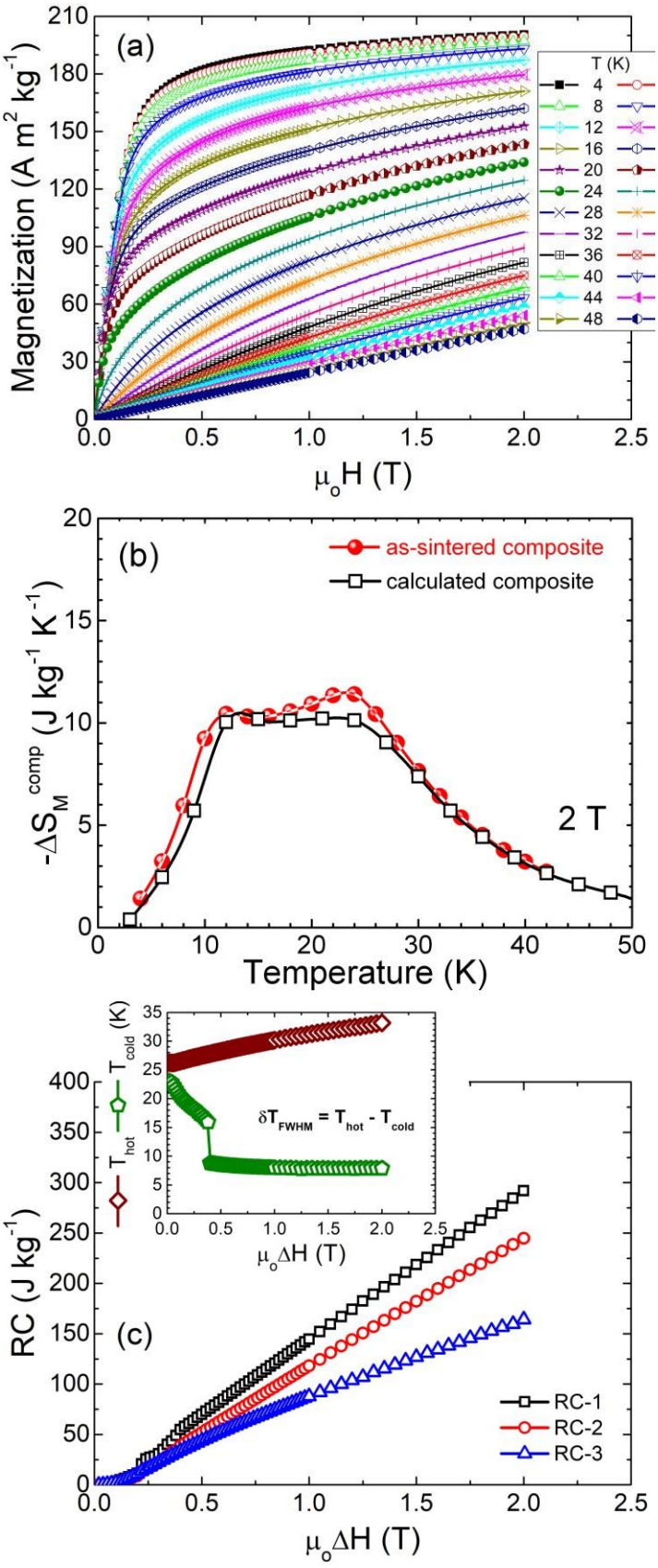
(a)
Magnetization (A m^2 kg^{-1})
μ_oH (T)
T (K)
4
8
12
16
20
24
28
32
36
40
44
48
(b)
as-sintered composite
calculated composite
2 T
$-\Delta S_M^{comp}$ (J kg^{-1} K^{-1})
Temperature (K)
T_{cold} (K)
T_{hot}
$\delta T_{FWHM} = T_{hot} - T_{cold}$
$\mu_o\Delta H$ (T)
(c)
RC (J kg^{-1})
RC-1
RC-2
RC-3
$\mu_o\Delta H$ (T)

Fig. 8.

***Declaration of Interest Statement**

Declaration of interests

☒ The authors declare that they have no known competing financial interests or personal relationships that could have appeared to influence the work reported in this paper.

☐The authors declare the following financial interests/personal relationships which may be considered as potential competing interests: